Multi-material Joining of an Aluminum Alloy to Copper, Steel, and Titanium by Hybrid Metal Extrusion & Bonding

TINA BERGH, HURSANAY FYHN, LISE SANDNES, JØRGEN BLINDHEIM, ØYSTEIN GRONG, RANDI HOLMESTAD, FILIPPO BERTO, and PER ERIK VULLUM

Hybrid metal extrusion & bonding (HYB) is a solid-state welding method where an aluminum (Al) filler wire is continuously extruded into the weld groove between the metal parts to be joined by the use of a rotating steel tool that provides friction and plastic deformation. Although the HYB method was originally invented for Al joining, the process has shown great potential also for multi-material joining. This potential is explored through characterization of a unique Al–copper–steel–titanium (Al–Cu–steel–Ti) butt joint made in one pass. Each of the three dissimilar metal interface regions are characterized in terms of microstructure and tensile properties. Scanning and transmission electron microscopy reveals that bonding is achieved through a combination of nanoscale intermetallic phase formation and microscale mechanical interlocking. Electron diffraction is used to identify the main intermetallic phases present in the interfacial layers. Machining of miniature specimens enables tensile testing of each interface region. Overall, the presented characterization demonstrates the great potential for multi-material joining by HYB and provides fundamental insight into solid-state welding involving bonding of Al to Ti, steel, and Cu.

I. INTRODUCTION

MULTI-MATERIAL or hybrid structures consist of two or more dissimilar materials that are joined together, which allow the properties of the parent materials to be jointly exploited.[1] Multi-material joints enable optimization of the material selection in each individual structural component and can be used to improve functionality or performance and/or to reduce weight or cost.[2] With such joints, lighter structures that retain high load-bearing capacities can be achieved,[3] which are crucial in reducing the environmental footprint in transportation industries. A prime example is joints between aluminum (Al) alloys and steels. They combine the light weight of Al alloys with the high strength of steels and enable improvement of the strength to weight distribution in, *e.g.*, automotive components.[4] Furthermore, titanium (Ti) and its alloys have excellent corrosion resistances and high specific strengths that can be retained at high temperatures. They are, therefore, commonly used in the aerospace industry, often together with lightweight materials such as Al alloys.[5,6] Moreover, both Al and copper (Cu) have high electrical conductivity, and substituting Al with Cu by the use of Al–Cu joints may offer great weight and cost saving potential for electrical devices.[7] To realize use of such multi-material components, cost-effective, robust, and flexible welding methods capable of joining dissimilar materials without significantly deteriorating their properties are crucial.

Dissimilar metal welding is challenging due to the differences in thermo-physical properties between the materials to be joined. Also, brittle intermetallic phases (IMPs) may form along the bonded interfaces.[8,9] In particular, the phases θ-Fe$_4$Al$_{13}$ and η-Fe$_2$Al$_5$,[10,11] θ-CuAl$_2$ and γ_1-Cu$_9$Al$_4$,[12] and TiAl$_3$,[13,14] often form during welding of Al–steel, Al–Cu, and Al–Ti, respectively. Studies have showed that as the IMP layer

TINA BERGH is with the Department of Chemical Engineering, Norwegian University of Science and Technology (NTNU), 7491 Trondheim, Norway and also with the Department of Physics, NTNU, 7491 Trondheim, Norway. Contact e-mail: tina.bergh@ntnu.no HURSANAY FYHN and RANDI HOLMESTAD are with the Department of Physics, NTNU. LISE SANDNES, JØRGEN BLINDHEIM, ØYSTEIN GRONG, and FILIPPO BERTO are with the Department of Mechanical and Industrial Engineering, NTNU, 7491 Trondheim, Norway. PER ERIK VULLUM is with the Department of Physics, NTNU and also with the SINTEF Industry, 7034 Trondheim, Norway.

thickness increases, the joint strength decreases in Al–steel,[15,16] Al–Cu,[9,17] and Al–Ti[18,19] joints. Conversely, a thin IMP layer contributes to low interfacial electrical resistivity for Al–Cu joints.[17,20] The growth of IMP layers is often diffusion controlled, both for Al–Fe,[21] Al–Cu,[9,22,23] and Al–Ti layers.[13,24] Thus, the IMP layer growth typically accelerates at elevated temperatures, so that welding with low heat input is necessary. Limiting the heat input is also advantageous for welding of Al alloys in general. This is because both age-hardened and work-hardened Al alloys are sensitive to reheating and often develop a soft heat-affected zone following welding which may reduce the overall joint strength.

Important solid-state welding methods include, *e.g.*, cold-pressure welding and friction stir welding (FSW) techniques.[25,26] The solid-state welding method hybrid metal extrusion & bonding (HYB) was developed more recently[27,28] and was originally designed for butt joining of Al plates and profiles.[29–31] The HYB method relies on filling the weld groove between the base materials (BMs) to be joined with a solid filler metal (FM), based on the principles of continuous extrusion. A specially designed extruder tool is used that comprises a non-consumable rotating steel pin equipped with a set of moving extrusion dies at the bottom end.[29] During HYB, the extruder tool travels along the weld line, and a filler wire is fed into the tool and subsequently becomes forced to flow out of the extrusion dies and into the groove behind the pin. At the same time as freshly extruded FM is deposited, the rotating steel pin typically deforms the edge of at least one of the BMs and drags it into the weld groove. This combination of continuous extrusion, friction, and plastic deformation is the fundamental working principle of the HYB method. The method is flexible and allows various joint configurations.[28,32] It can also be used as a basis for additive manufacturing of small parts by depositing the Al FM in a layer-wise manner.[33] Due to the low process temperature and flexibility, the HYB method has shown great potential also for dissimilar metal welding. Three generations of Al–steel HYB butt joints have been characterized, and they showed progressively improved tensile properties.[34–36] Furthermore, it was recently reported that HYB offers the rare capability of producing multi-material Al–steel–Ti and Al–Cu–steel–Ti joints in one pass.[28,32] Previous characterization of HYB joints has included Al–Al, Al–steel, and Al–Cu HYB butt joints, but similar types of exploratory studies are also needed for other types of HYB joints with different geometries and/or other BM combinations.

This article focuses on exploring the feasibility of multi-material HYB joining. Microstructural and mechanical characterization of a unique four-metal Al–Cu–steel–Ti HYB joint that was welded in one pass is presented for the first time. In this joint, Cu and Ti BM plates were placed in a butt configuration, while a steel BM plate was placed below them. The Al FM was then deposited in the groove in between these BMs, which allowed Al to bond to each of the three BMs. Although this demonstration joint has no direct application in industry to date, disclosure of its metallurgical characteristics provides invaluable insights into Al–Cu and Al–Ti HYB butt joining, and Al–steel HYB lap joining. The focus of this work is placed on understanding of the underlying bonding mechanisms and evaluation of the local tensile properties of the three dissimilar metal interface regions. The overall aim is to provide new information about multi-material HYB joining, which may be used to better understand and further improve solid-state welding of Al to Cu, steel, and Ti in general.

II. MATERIALS AND METHODS

A. *Materials*

The multi-material joint was made using a filler wire of Al alloy 6082. The wire had been homogenized, hot extruded, shaved, and cold drawn to reach its final diameter of ∅1.4 mm. The composition is listed in Table I. The three BM plates were each 100 mm wide and 250 mm long. They included a 3-mm-thick plate of commercially pure half-hard Cu (Cu-0.5 H; ≥99.9 wt pct Cu), a 1.5-mm-thick plate of galvanized dual-phase steel HCT590, and a 3-mm-thick plate of unalloyed Ti of grade 2 (≥99.2 wt pct Ti). Prior to the welding operation, the galvanized surface layer on the steel BM that would be in contact with the FM was removed by machining to prevent any influence of the zinc layer on the formation of the IMPs. Subsequently, the three BM plates were cleaned with acetone to remove remnants of oil and grease from the exposed surfaces to be bonded.

B. *Hybrid Metal Extrusion & Bonding*

Prior to joining, the BMs were clamped on top of the HYB workbench. The Cu and Ti BMs were fastened on top of the steel BM, with a 8.6-mm-wide I-groove between them. The Ti BM was placed on the advancing side (AS), where the welding direction was the same as the pin rotation direction, while the Cu BM was placed on the retreating side (RS), in accordance with the nomenclature used for FSW.[25] A 9 mm in diameter pin was positioned so that it should not deform the steel and Ti BMs but slightly machine the Cu BM during joining.

During HYB, the extruder tool traveled along the weld line, at the same time as the filler wire was fed into the extruder tool. Inside the extruder, the Al filler wire was pressed into the narrow space between the stationary steel housing and the rotating pin, which acted as an extrusion chamber. Frictional forces stemming from the three rotating pin walls caused the Al FM to become dragged along with the pin. At the back side of the extrusion chamber, the Al FM met an abutment that forced it to be extruded through the moving dies in the lower end of the pin and into the weld groove. In this case, the rotating steel pin had four moving extrusion dies at its lower end. Figure 1(a) shows a front-view illustration of the process, while (b) shows a top-view sketch. The Al FM was dragged along with the pin towards the RS, before it became deposited in the groove behind the pin and bonded to each of the three

Table I. The Composition of the Al Filler Wire Given in Wt Pct.

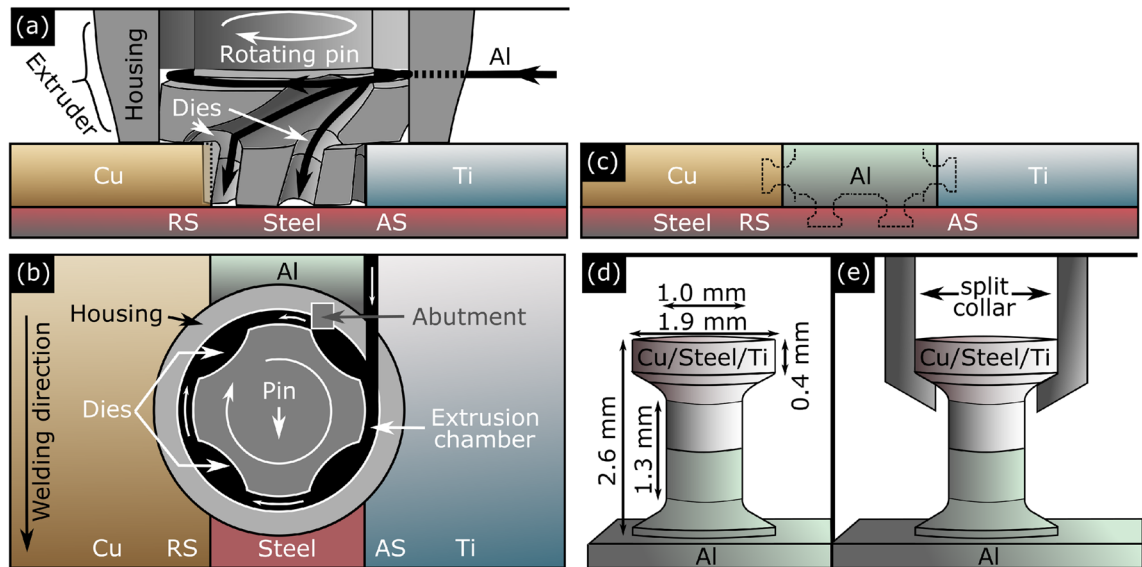| Si	Mg	Mn	Fe	Cr	Cu	Ti	Zr	B	Other
1.11	0.61	0.51	0.2	0.14	0.002	0.043	0.13	0.006	0.029

Fig. 1—Sketch (not to scale) of the HYB process and the miniature tensile testing. Illustrations of the setup (*a*) and (*b*) during, and (*c*) after HYB. (a) and (c) show front-views, while (b) shows a top-view of a section through the extrusion chamber. Before HYB, the Cu, Ti, and steel BMs were fastened so that a 8.6-mm-wide I-groove was formed between Cu and Ti. During HYB, the extruder tool traveled along the BMs [down in (b)], while Al was extruded through dies in the rotating pin after meeting an abutment. Al FM was deposited in the groove and bonded to each of the BMs, and a finished joint was produced after HYB. Tensile specimens were fabricated for each dissimilar metal interface region, as illustrated in (c). Illustration of one miniature tensile specimen where (*d*) its dimensions are given, and (*e*) the specimen is fastened with clamps and tensile loaded using a split collar.

BMs in the finished multi-material joint, as illustrated in Figure 1(c). Further descriptions of the material flow during butt welding by HYB can be found in other publications.[37] Note that in this joint, the Al FM acted as a solid-state solder, and hence, the three BMs were not directly bonded to each other.

The joining parameters used were pin rotation speed: 350 RPM, welding speed: 6 mm/s, and wire feed rate: 115 mm/s. During the joining process, cooling of the Al filler wire inlet hole in the non-rotating housing enclosing the rotating pin was performed by spraying with dry ice supplied at a rate of 160 g/min. The gross heat input was estimated to be 0.33 kJ/mm.

C. Mechanical Characterization

To study the effect of HYB on the BMs, hardness measurements were conducted on a polished cross section according to the standard ASTM E92-17.[38] This was done using a Mitutoyo micro-Vickers hardness testing machine with an applied load of 1.0 kg. Two horizontal profiles were measured: one that sampled the Cu–Al–Ti region and one that sampled the steel. Vertical profiles that sampled the Al–steel region were also measured. The specimen was mechanically polished after measuring each profile, to allow for multiple

measurements. In total, three individual sets of hardness profiles were measured at each of the three locations.

To assess the bond strengths, tensile testing of each of the three dissimilar metal interface regions were performed individually. Miniature tensile test specimens were made and measured using the testing setup developed by Blindheim et al.[39] A Mazak 3-axis vertical machining center mill was used to machine cylindrical specimens, as illustrated in Figure 1(c). Fourteen specimens were made from the Al–Cu interface region and seven from the Al–Ti interface region. For the Al–steel region, three specimens were made from the RS (towards Cu) and three from the AS (towards Ti). The diameter of the middle section of the cylindrical tensile specimens, which sampled the dissimilar metal interfaces, was 1.0 mm. The diameter of their top and bottom regions was 1.9 mm, as illustrated in Figure 1(d). Prior to testing, the specimens were clamped to the test machine, and a specially designed split collar tool was used to grip each specimen, as shown schematically in Figure 1(e). To record the applied load and total displacement during testing, a MTS Criterion Model 42 ball screw universal testing machine was used employing a cross-head speed of 1 mm/min and a sampling frequency of 10 Hz. After tensile testing, the fracture surfaces were studied by
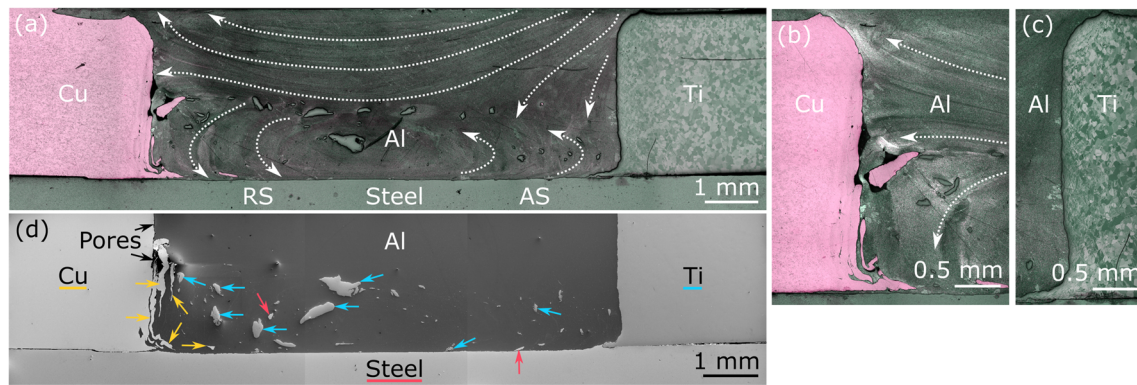
Fig. 2—Overview of the joint cross section. (*a*) Optical micrograph of a leached cross section, where the Al FM flow pattern is indicated by white lines. Higher magnification optical micrographs of the (*b*) Al–Cu and (*c*) Al–Ti interface regions. (*d*) SE-SEM image of a mechanically polished joint cross section. The arrows colored blue, red, and yellow pinpoint Ti, steel, and Cu fragments located within the Al FM, respectively (Color figure online).

scanning electron microscopy (SEM) using the same conditions as outlined in Section II–D.

D. *Microstructural Characterization*

For optical microscopy, a polished cross section of the joint was leached in a solution of 100 mL H_2O and 1 g NaOH for 3 to 4 minutes and subsequently imaged using an Alicona confocal microscope.

Mechanically polished cross sections were imaged by SEM using a Zeiss Supra 55 VP operated at acceleration voltages in the range of 10 to 20 kV. Both secondary electron (SE) and backscattered electron (BSE) images were acquired. Each dissimilar metal interface region was studied to reveal formation of IMP layers. Fragments of the BMs embedded within the Al FM were characterized by X-ray energy dispersive spectroscopy (EDS) point analysis using an EDAX Octane Pro detector.

Cross sectional lamellae from each of the three interface regions; Al–Cu, Al–Ti, and Al–steel, were prepared by focused ion beam (FIB) lift-out using a dual-beam FEI Helios G4.

(Scanning) transmission electron microscopy [(S)TEM] and EDS mapping were performed using a JEOL ARM200F integrated with CEOS spherical aberration correctors and a Centurio EDS detector, operated at 200 kV. The EDS maps were analyzed using the python library hyperspy.[40] The data analysis involved model fitting of each spectrum with a model comprising a sixth-order polynomial to model the background and one Gaussian per X-ray line identified. Afterwards, the Cliff–Lorimer quantification method was used to convert the X-ray line intensities extracted from the model fitting to atomic percentages (at. pct) using calculated *k*-factors.

Electron diffraction was performed to assess the crystal structures of the phases comprising the interfacial IMP layers. Zone-axis selected area electron diffraction (SAED) patterns were recorded using a JEOL JEM2100 operated at 200 kV. A JEOL JEM2100F fitted with a NanoMegas ASTAR system was used to collect zone-axis precession electron diffraction (PED) patterns

and scanning PED (SPED) datasets. For (S)PED, the microscope was operated at 200 kV in nanobeam diffraction mode, using a convergence semi-angle of 1 mrad, a precession angle of 17 mrad, and a precession frequency of 100 Hz. The zone-axis PED patterns were recorded on an Ultrascan charge-coupled device camera. The SPED datasets were acquired on a Merlin Medipix direct electron detector with 256×256 pixels, and the exposure time was 10 ms per pattern. The SPED data were visualized and analyzed using the python library pyxem.[41] PED patterns in the SPED datasets originating from interfacial IMP crystals oriented close to zone axes were identified manually and analyzed further. All the recorded SAED and PED zone-axis patterns and the selected close to zone-axis PED patterns were analyzed by measuring the angles and distances between Bragg spots in calibrated units (Å^{-1}). The patterns were then attempted indexed with respect to all the candidate crystal structures selected from the literature. The Al–Cu, Al–Fe, Al–Fe–Si, and Al–Ti(–Si) crystal structures that were considered as candidates are tabulated in Tables S-I, S-II, S-III, S-IV, and S-V (refer to electronic supplementary material), respectively.

III. RESULTS

A. *Microstructural Characterization*

An overview of the joint cross section is shown in Figure 2, where (a) shows an optical micrograph where the Al FM flow pattern is indicated. Figure 2(b) displays an optical micrograph of the Al–Cu interface region. The upper and middle parts contained gaps and voids, and detached Cu fragments were embedded within the Al FM. The Al–Ti interface region is shown in Figure 2(c), where it can be seen that the Ti grains are smaller closer to the Al interface. The joint cross section was also imaged by SEM, and Figure 2(d) shows an overview image. While both the Al–Ti and the Al–steel couples seemed tightly bonded, a gap could be seen in the upper part of the Al–Cu interface. Furthermore, EDS point analysis revealed that most of the BM
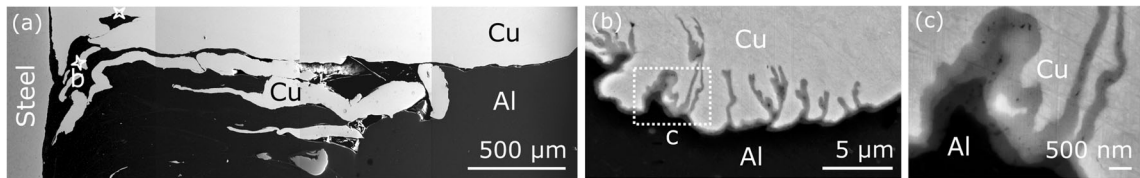
Fig. 3—SE-SEM images of the Al–Cu interface showing (*a*) an overview of the Al–Cu region, and (*b*) and (*c*) the Al–Cu IMP layer at the location indicated with a white star marked 'b' in (a). The upper white star in (a) indicates the location from where the lamella shown in Fig. 4 was lifted out. Note that the displayed images are rotated clockwise 90° relative to those shown in Fig. 2.
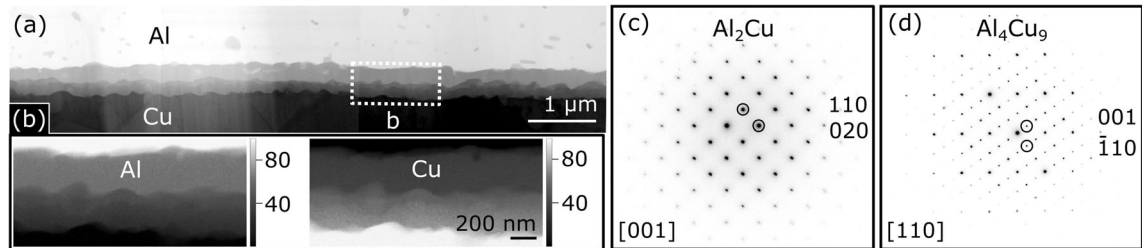

Fig. 4—TEM of the Al–Cu interface region. (*a*) Overview BF-STEM image. (*b*) Element maps based on STEM EDS showing at. pct, from a TEM lamella lifted out from the region marked with the upper white star in Fig. 3(a). SAED patterns from: (*c*) a θ-Al$_2$Cu crystal oriented to zone axis [001], and (*d*) a γ_1-Al$_4$Cu$_9$ crystal oriented to zone axis [110].

fragments embedded within the Al FM originated from the Ti, while there were a few from the Cu and the steel, as indicated with the colored arrows in the image. Large variations were observed along the groove walls both with respect to the occurrence of fragmented BM pieces and voids along the Al–Cu interface. Such variations can be seen, *e.g.*, by comparing Figures 2(a) and (d).

1. The Al–Cu interface region

SEM images of the Al–Cu interface are shown in Figure 3, where (a) presents an overview and (b) and (c) show higher magnification SE images. A continuous ~0.5 μm thick IMP layer covered the bonded Al–Cu interfaces. Figure 4(a) shows a bright-field (BF)-STEM overview image where it can be seen that the IMP layer consists of two individual layers with distinct compositions. The layer closest to Al was 221 ± 48 nm thick (average and one standard deviation), while that closest to Cu was 189 ± 30 nm thick within the imaged TEM lamella. Element maps based on STEM EDS are shown for Al and Cu in Figure 4(b). Corresponding element maps for elements present in small amounts (Si, Mn, and Ti) are shown in Figure S-1, where smaller Al–Si–Mn and Al–Si–Ti dispersoids also can be seen. The two Al–Cu layers were estimated to contain 36 and 68 at. pct Cu. These values lie on the Cu-rich side of the reported homogeneity ranges for the phases Al$_2$Cu and Al$_4$Cu$_9$ of 32 to 33 and 65 to 69 at. pct Cu, respectively, at 400° C.[42] In the present case, the Cu content is most likely overestimated due to absorption of low energy Al Kα X-rays. Further, TEM showed that in more deformed interface regions with a slightly thicker IMP layer, there was a third thinner layer that appeared between Al$_2$Cu and Al$_4$Cu$_9$ with intermediate contrast.

SAED was performed to identify the two main Al–Cu phases constituting the IMP layer. The SAED patterns recorded from the first layer, such as that shown in Figure 4(c), could all be indexed with respect to the phase θ-Al$_2$Cu ($I4/mcm$ (140), $a = 6.06, c = 4.87$ Å[43]). The patterns recorded from the second layer all fit the phase γ_1-Al$_4$Cu$_9$ ($P\bar{4}3m$ (215), $a = 8.70$ Å[44]), and Figure 4(d) shows an example pattern. Section S-1 lists the Al–Cu phases considered as candidates, while Section S-4 shows additional indexed SAED patterns from these two phases. The γ_1 phase has been found to undergo a rhombohedral distortion at lower Cu contents, designated as the δ phase,[45] but the single-phase regions of δ and γ_1 have not been determined.[42,46,47] Since it was not possible to conclude whether the Al$_4$Cu$_9$ phase was distorted or not, the recorded SAED patterns were all indexed with respect to the cubic γ_1 phase although they fit both δ and γ_1.

2. The Al–steel interface region

Figure 5 shows an overview SE-SEM image of the Al–steel interface. SEM indicated bonding along the whole weld line, and no gaps were seen. Figure 5(b) and (c) depicts the RS and AS, respectively, where the AS can be seen to have a more deformed interface with mechanically intermixed Al–steel areas. For instance, the area shown in Figure 5(d) resembles a layered structure. An IMP layer was also observed, and the layer was typically thicker on the AS, where it reached up to a few μm at most.

An overview BF-STEM image of an Al–steel region from the middle of the weld is presented in Figure 6(a). The thickness of the IMP layer varied from 93 ± 20 nm (average and one standard deviation) in the thin part and up to ~1 μm in the thicker and more irregular parts.
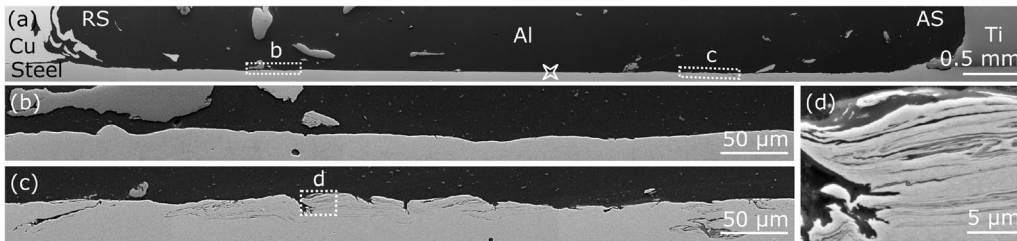
Fig. 5—SEM of the Al–steel interface region. (a) Overview SE-SEM image, where the white star marks the position from where the TEM lamella pictured in Fig. 6 was lifted out. Higher magnification SE-SEM images of the Al–steel interface region from the (b) RS (Cu side) and (c) AS (Ti side). (d) Higher magnification image showing a layered intermixed region where an IMP layer had formed along the Al–steel interface.
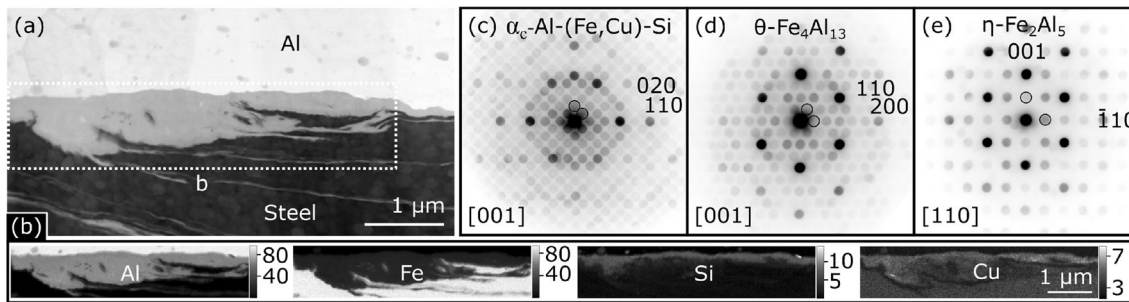

Fig. 6—TEM of the Al–steel interface region. (a) Overview BF-STEM image and (b) element maps based on STEM EDS, showing at. pct. Zone-axis PED patterns from: (c) the cubic α_c-Al–(Fe,Cu)–Si phase oriented to zone axis [001], (d) the θ-Fe$_4$Al$_{13}$ phase oriented to zone axis [001], and (e) the η-Fe$_2$Al$_5$ phase oriented to zone axis [110].

Also, some IMP layer lines extended several μm into the steel. The steel grains were equiaxed and ~0.2 μm wide close to the interface. Element maps based on STEM EDS from a region with a thick IMP layer are shown in Figure 6(b) for Al, Fe, Si, and Cu and for other elements (Mn, O, Cr, Ti, and Mg) in Figure S-4(b). Figure S-4(c) shows element maps from a region with a thin IMP layer. The IMP layer was mainly composed of Al, Fe, Si, and Cu, and in the thicker parts the Si and Cu contents increased towards the Al interface.

To identify the main phases present in the IMP layer, zone-axis PED patterns were indexed with respect to the candidate Al–Fe and Al–Fe–Si crystal structures listed in Tables S-II and S-III. The patterns from crystals adjacent to Al were consistent with the cubic α_c-Al–(Fe, Cu)–Si phase ($Im\bar{3}$ (204), $a = 12.56$ Å[48]), as shown in Figure 6(c) for zone axis [001]. In thinner parts of the IMP layer (~0.1 μm), only the α_c phase was present. Patterns from the middle region of the IMP layer also proved the presence of the θ-Fe$_4$Al$_{13}$ phase, and Figure 6(d) shows a pattern from this phase oriented to zone axis [001]. When it came to patterns from grains in the IMP layer that were located adjacent to the steel, these were consistent with the η-Fe$_2$Al$_5$ phase, as shown for zone axis [110] in Figure 6(e). Additional zone-axis patterns from each of these three phases are shown in Figures S-5 and S-6.

3. The Al–Ti interface region

An overview SE-SEM image of the Al–Ti interface is shown in Figure 7(a). Large portions of the interface appeared sharp without any indications of IMP layers

or gaps, while a few areas contained mechanically intermixed Al–Ti areas with thin IMP layers, as can be seen from Figure 7(b). An overview BF-STEM image is shown in Figure 8(a), where both sharp and highly deformed intermixed regions can be seen. A continuous ~50 nm thick IMP layer covered the Al–Ti interface. Element maps based on STEM EDS are shown in Figure 7(b), which reveal that the IMP layer mainly consists of Al, Ti and Si. The dispersoids in the Al FM close to the interface were also mainly composed of Al, Ti and Si, while a few particles were rich in either Cu, or Si, Mn, Cr and Fe, or Mg and Si, or P. An example of the latter is shown in Figure S-8, which contains additional maps from elements present in small amounts (O, Mn, Cr, Fe, Mg, and P). Element maps from a thicker intermixed region are shown in Figure S-7.

Due to the small size of the individual crystals in the Al–Ti–Si IMP layer, it was impossible to acquire conventional zone-axis diffraction patterns. Instead, SPED datasets were collected with various specimen tilt conditions, and the data were manually inspected to select patterns from IMP crystals oriented close to zone axes. The selected patterns were attempted indexed with respect to the candidate Al–Ti(–Si) structures listed in Table S-IV. Some of the selected patterns were consistent with the Bragg spot geometry of several of the candidates. Nevertheless, there were a few patterns that only fit the phase TiAl$_3$ ($I4/mmm$ (139), $a = 3.84$, $c = 8.58$ Å,[49,50]) such as those shown in Figures 8(c) and (d). Additional PED patterns indexed with respect to this phase are shown in Figure S-7.
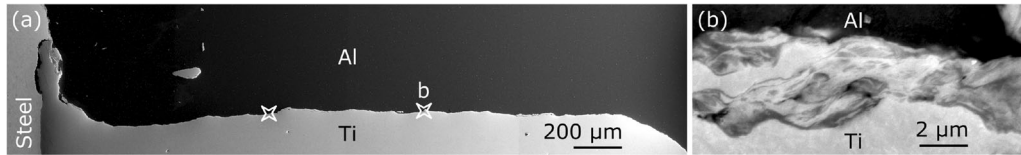
Fig. 7—SE-SEM images of the Al–Ti interface region. (*a*) Overview image, and (*b*) higher magnification image of an intermixed region from the location indicated by the white star marked 'b' in (a). The left star in (a) marks the location from where the lamella shown in Fig. 8 was lifted out.
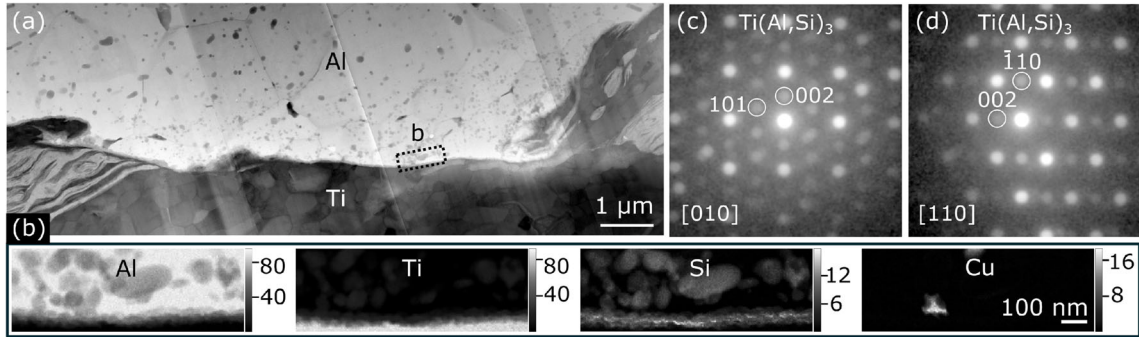

Fig. 8—TEM of the Al–Ti interface region from the location marked by the left white star in Fig. 7(a). (*a*) Overview BF-STEM image. (*b*) Element maps based on STEM EDS showing the relative composition in at. pct, from the region marked in (a). PED patterns from IMP crystals that were selected from SPED datasets and indexed with respect to the $Ti(Al,Si)_3$ phase oriented close to zone axis: (*c*) [010] and (*d*) [110].
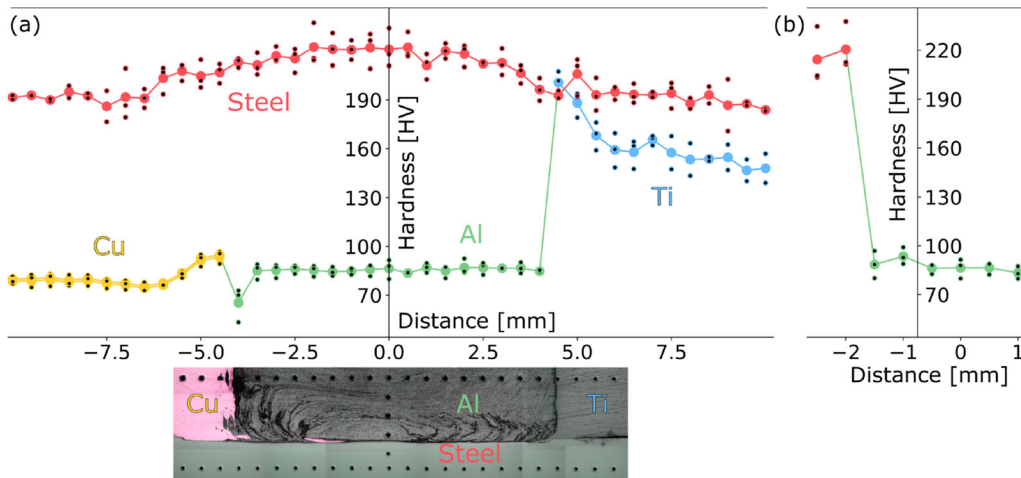

Fig. 9—Hardness profiles. (*a*) Horizontal hardness profiles measured across the Cu–Al–Ti and steel regions. The bottom inset displays an optical micrograph of an indented region. (*b*) Vertical hardness profiles measured across the Al–steel region. In total, three profiles were measured from each region, and the black dots show the individually measured values, while the colored dots connected by lines show the average values.

B. Mechanical Characterization

1. Hardness measurements

Horizontal hardness profiles measured along the joint cross sections are shown in Figure 9(a). Note that the dip in the Cu–Al curve at −4.0 mm corresponds to the location of large voids. Vertical hardness profiles measured across the Al–steel region are presented in Figure 9(b). The Al FM showed a relatively flat hardness curve, 86 $HV_{1.0}$ in average, in both the horizontal and vertical profiles, which is lower than the initial hardness of the Al filler wire measured to 125 ± 2 $HV_{0.5}$.[35] The hardnesses of both Ti and Cu increased towards their interfaces to Al; from an average of 155 ± 6 $HV_{1.0}$ to 201 $HV_{1.0}$ next to the Al interface for Ti, and from 79 ± 2 $HV_{1.0}$ to 95 $HV_{1.0}$ for Cu. The hardness of the steel increased from ~190 $HV_{1.0}$ in the BM to ~220 $HV_{1.0}$ in the middle of the weld groove.

2. Tensile testing

To assess the bond strengths, miniature tensile specimens were machined from each of the three dissimilar metal interface regions. All of the 14 Al–Cu specimens fractured during machining or mounting in the test machine, as a consequence of the presence of voids and gaps along the Al–Cu interface and the high stresses experienced during specimen machining. The Al side of the fracture surfaces showed complex deformed topographies with several bumps and bulges that resembled the flow of the Al FM, as shown in Figure 10(a). All of the Cu fracture surfaces were damaged, except one which is shown in Figure 10(b). This Cu surface was largely flat with some dent lines. However, residual Al can be seen in the region to the left in Figure 10(b), which confirms that Al is bonded to Cu in some areas.

For the Al–steel specimens, the force–displacement curves obtained from miniature tensile testing are shown in Figure 11(a). All specimens showed evidence of brittle fracture initiation. For the AS specimens, the average UTS was 286 ± 22 MPa, which was higher than the average UTS of 228 ± 17 MPa measured for the RS specimens. Figure 11(b) and (c) shows side-view SEM images of the steel side and the Al side of one fractured

tensile specimen, respectively. They stem from the same fractured specimen sampling the AS, and corresponding locations on the two sides are indicated by colored circles in the figure. Top-view images of the same surfaces are shown in Figures 11(d) and (e). The fracture surfaces mostly appear medium gray, although some steel and some Al regions can be seen at both of them. This indicates that the fracture had mainly propagated not only through IMP or intermixed regions, but also partly through some of the adjacent Al and steel regions.

The force–displacement curves obtained from tensile testing of the Al–Ti specimens are shown in Figure 12(a). All specimens showed ductile behavior with necking and fracture occurring in Al. The maximum force was 240 ± 2 N (average and one standard deviation), corresponding to an UTS of 306 ± 2 MPa. Figure 12(b) and (c) shows side-view SEM images of the Ti side and the Al side, respectively, of one fractured

Fig. 12—Miniature tensile testing of Al–Ti specimens. (a) Force–displacement curves obtained via tensile testing. The horizontal black line indicates the average fracture force, while the light gray horizontal line shows plus and minus one standard deviation. (b) and (c) BSE-SEM images of one fractured Al–Ti tensile specimen, where (b) shows the Ti part of the fractured specimen and (c) shows the Al part.
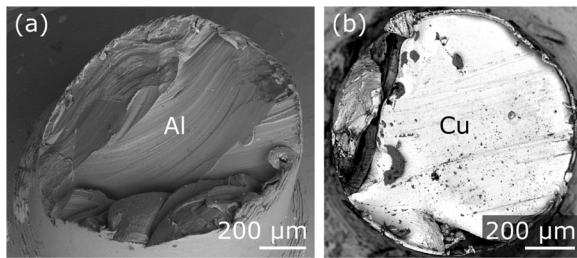

Fig. 10—BSE-SEM images of the fracture surfaces from two Al–Cu tensile test specimens that fractured before testing. (a) shows the Al side of one fracture surface imaged slightly from the side, while (b) shows the Cu side of another fracture surface viewed from the top.
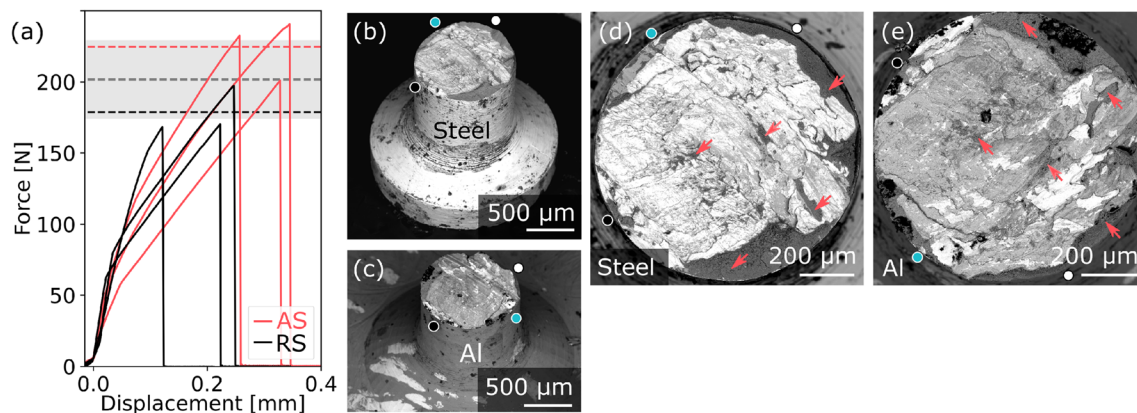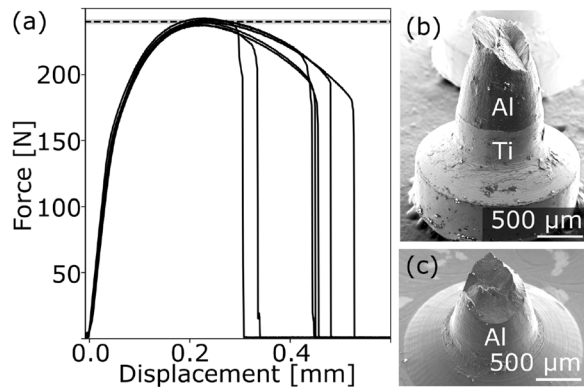

Fig. 11—Miniature tensile testing of Al–steel specimens. (a) Force–displacement curves obtained from tensile testing of specimens from the AS (red) and the RS (black). The dashed lines show the average peak forces for AS (red) and RS specimens (black) and for all specimens (gray). The gray region indicates the spread (plus and minus one standard deviation) in the average peak force calculated for all the tensile specimens. (b) and (c) BSE-SEM images of the steel and the Al side of one fractured tensile specimen, respectively, imaged from the side. (d) and (e) BSE-SEM images of the same steel and Al fracture surfaces, respectively, imaged from the top. The colored circles mark corresponding locations on the various images, and at some locations, Al is marked with red arrows (Color figure online).

Al-Ti tensile specimen. Necking had occurred in Al, and the fracture surfaces had slanted edges and showed dimples at higher magnifications, supporting the presumption of ductile fracture development.

IV. DISCUSSION

A. *The Material Flow Inside the Extrusion Zone*

The observed flow pattern inside the extrusion zone (Figure 2) reveals that HYB is asymmetric with respect to the material flow on the AS compared to the RS. Specifically, it can be seen that the material on the top of the AS (Ti side) flowed downward towards the middle, before it flowed upwards again on the RS (Cu side). In the lower region of the weld, the Al flow pattern is more complex and onion-like. This resembles the material flow in FSW, where a recent study on Al–Al FSW showed that the material flowed downward on the AS and upwards on the RS, before it flowed to the back of the tool along the RS.[51] Due to the asymmetry in the material flow patterns both for HYB and FSW, the positioning of the pin with respect to the center line of the weld along with the placement of the dissimilar BMs on either the AS or the RS will have a strong influence on the joint properties.[52] The largest difference between HYB and FSW in this regard is that the Al FM addition in the HYB case allows for the use of a groove between the BMs. This provides a greater flexibility when it comes to positioning of the pin with respect to the various BMs involved and choice of joint configuration. Typically in HYB butt welding, the pin is placed so that it mainly deforms the softest BM which is placed on the RS. This asymmetric positioning of the pin inside the groove means that the softest BM becomes stirred and dragged towards the middle of the weld groove before it is deposited behind the pin.[37] On the other hand, the role of the pin on the AS is to break up or machine off the surface oxide layer on the hardest BM before it comes into contact with the downward flowing freshly extruded Al FM. This HYB setup geometry has been shown to provide the best conditions for achieving a sound metallurgical bond between dissimilar metals.[35]

In the present setup, the Cu BM was placed on the RS, since it was the softest BM. The pin was positioned so that it would only slightly deform the Cu BM without machining the Ti or steel BMs. This is essential to keep the heat input low and avoid accumulation of hard BM fragments inside the Al FM. In FSW, an increasing number of large BM fragments are typically seen in dissimilar welds with increasing tool offset towards the harder BM, and these fragments may constitute a preferred path for crack propagation.[53] Also in the present case, several BM fragments were observed within the Al FM (Figure 2(d)), which implied that the rotating steel pin had scribed or machined the BM surfaces. This is believed to be caused by tool vibrations during the welding operation.[36] In addition, several voids and gaps were seen close to the Al–Cu interface, which occurred due to insufficient Al FM feeding. This, in turn, mainly happened as a consequence of the chosen joint geometry, with the Cu BM placed on the RS in combination with the use of a small 0.4 mm overlap between the Cu BM and the pin. This geometry confined the material flow that typically occurs in HYB butt welding, as discussed previously. On the other hand, sound Al–Cu HYB butt joints have recently been demonstrated for the case where the Cu BM is placed on the AS and the Al BM on the RS, in combination with a 3 mm pin offset towards the RS.[54] This agrees well with previous studies reporting that sound FSW Al–Cu joints can be produced if Cu is placed on the AS, whereas Cu placed on the RS may lead to defects.[55,56] Still, it is believed that the bonding conditions in the HYB case can be improved also with the Cu BM placed on the RS by proper adjustment of the Al FM feed rate.[32]

B. *The Thermo-mechanically Affected Zones*

The hardness profiles (Figure 9) reflect the extent of thermo-mechanical processing that occurred within the three BMs and the FM during HYB. The extrusion zone lies in the middle of the weld, similar to the stir zone in FSW.[26] Significant softening of the cold-worked Al filler wire happened as it passed through the extruder. This reflects the high temperatures it experienced both inside the extrusion chamber and in the weld groove immediately below the pin shoulder, where it has been reported to reach peak temperatures of about 400° C[57] and 460 °C,[58] respectively. The observed drop in hardness most likely occurred due to a decrease in dislocation density and an elimination of the work hardening introduced by the cold drawing of the filler wire employed in the last manufacturing step. Note that the softening is not believed to be caused by coalescence and/or dissolution of precipitates, since the Al filler wire has not been artificially aged to form strengthening precipitates. At the same time, the high content of dispersoid forming elements, such as Cr and Zr, was believed to prevent recrystallization of the Al FM during heating.

On all three sides of the extrusion zone, the BMs were affected by the high extrusion pressure and the physical contact with the pin. Therefore, an increase in the hardness of the BMs could be seen towards the dissimilar metal interfaces. The observed hardness increase in the Cu BM was most likely caused by work hardening, as discussed in a recent study on HYB Al–Cu welds, where a similar hardness increase was observed.[54] In another study, the temperature in an Al BM placed on the RS reached a maximum of 275 °C, measured 3 mm from the outer pin edge during Al–steel butt welding by HYB.[58] Since Cu has higher thermal conductivity than Al, the peak temperature reached at an equivalent position inside the Cu BM was probably even lower in the present study. This makes softening due to dislocation annihilation unlikely and may explain why the plastic deformation imposed locally by the pin leads to a hardness increase in the Cu adjacent to the bonded Al–Cu interface.

When it comes to the steel BM, TEM showed that the steel grains were equiaxed and ~0.2 μm wide near the Al–steel interface in the middle of the weld groove

(Figure 6(a)). This is much smaller than the typical grain sizes of ~10 to 15 μm reported for similar dual-phase steels.[59,60] Previous studies on FSW have reported that the frictional heating and plastic deformation occurring during welding promote recrystallization and strain hardening in dual-phase steels, resulting in a fine-grained microstructure with higher hardness.[59–61] This can explain the gradual hardness increase in the steel towards the middle of the weld groove. Further, in a recent study on HYB Al–steel welding, where a steel backing plate was used, it was reported that the peak temperature in the backing plate was about 200 °C, measured 1.4 mm below its surface close to the weld center line.[58] Due to the similarity in the joint geometry and process parameters, the thermal gradient inside the steel BM in the present case was probably comparable to that reported in the previous study. This explains why the hardness increase in the steel BM was confined to the region adjacent to the Al–steel interface.

Moreover, the Ti BM showed a spike in the hardness profile and grain size reduction close to the Al FM (Figure 2). Similar findings have also been reported for FSW of commercially pure Al and Ti, where grain size refinement and hardness increase were observed in the Ti BM close to the Al interface.[62] In a previous study on Al–steel butt welding by HYB, the peak temperature in the steel BM placed on the AS was measured to be below 340 °C one mm from the Al–steel interface.[58] Since Ti has a thermal conductivity that is similar to that of steel, the peak temperature at an equivalent position in the Ti BM in the present case was probably comparable to that reported previously. This temperature is believed to be sufficiently high to promote recrystallization in commercially pure Ti, leading to a local hardness increase following grain size refinement.

C. The Multi-material Interface Regions

Irregular and deformed interface regions with mechanical intermixing, up to a few μm thick, were seen both for Al–Cu, Al–steel, and Al–Ti (Figures 3(b), (c), 5(c), (d), and 7(b)). Such mechanically intermixed layered or swirl-like areas are common in FSW joints and originate from the stirring action of the pin giving rise to large plastic deformation.[63] Such regions increase the bonded surface area and may contribute to bonding *via* microscale mechanical interlocking,[53] as indicated in a study on Al–Ti FSW joints.[64] However, such intermixed layers are typically associated with interfacial fracture if they are thick. Examples of this type of fracture have been reported for Al–Ti[65] and Al–steel[66] FSW joints that displayed several μm thick intermixed layered regions which contained IMP layers.

SEM and TEM revealed that IMP layers had formed at all of the three dissimilar interfaces (Figures 4, 6, and 8), which demonstrated metallurgical bonding *via* interdiffusion. The thicknesses of the IMP layers give insight into the thermal conditions at the multi-material interfaces during HYB, since IMP layer growth generally accelerates with higher heat input.[9,13,21–24] The miniature tensile specimens contained the characteristic interface structures including IMPs and intermixed layers

and provided information on the local bond strengths of each interface region. Still, they were not large enough to capture the macroscale tensile behavior of the weld, since the widths of the thermo-mechanically affected zones were on the mm scale.

The Al–Cu IMP layer was ~0.5 μm thick (Figures 3 and 4). For FSW Al–Cu joints, it has been reported that the tensile strength decreases rapidly with increasing thickness for thicknesses exceeding ~2.5 μm[20] or ~2 μm,[9] while sound joints have been reported for thicknesses in the range of ~0.3 to 3 μm.[67] Since the ~0.5 μm thick layer seen here was comparable to or thinner than these reported critical thicknesses, the IMP layer could be assumed to be thin enough to not be detrimental to the joint tensile properties. During *in situ* TEM interdiffusion at 300 °C, a ~0.5 μm thick IMP layer was reported to form within 5 minutes.[68] This indicates that the local heat input was low in the present weld. Moreover, in a recent study on Al–Cu HYB butt welds, an IMP layer as thin as 0.19 μm was reported.[54] This can most likely be attributed to the higher welding speed used, which has been shown to reduce the peak temperature in Al–steel HYB welds.[58] Further, they reported that both the IMP layer growth rate and the interface resistivity were lower for these HYB welds than for other Al–Cu welds described in the literature. This explains their excellent electrical properties.[54]

In the present weld, the steel BM was placed below the pin and experienced a range of conditions reaching from the AS near the Ti BM to the RS near the Cu BM. SEM indicated that both IMP layers and intermixed regions were more widespread on the AS (Figure 5), which lead to the conclusion that the metallurgical bonding conditions were better on the AS, as previously discussed. The large spread in the measured UTS values observed for the Al–steel tensile specimens can probably be ascribed to these variations between the AS and the RS, together with fluctuations in the Al FM supply and oscillations of the steel pin inside the groove. On average, the UTS was higher for specimens that sampled the AS than the RS, which suggests that some unbonded areas and/or defects were present on the RS, despite that no signs of such could be disclosed by SEM. In spite of the brittle fracture development, the UTS values are comparable to those previously reported for similar miniature specimens, where ductile fracture occurred in the Al FM.[39] This indicates that the measured Al–steel bond strength is close to the tensile strength of the Al FM. Further, an IMP layer with comparable thickness (0.1 to 1 μm) was found in a third-generation Al-steel HYB joint, where ductile fracture occurred in the Al during tensile testing[36]. Hence, the IMP layer thickness is not believed to be the limiting factor here. Recently, finite element simulations of the thermal field in HYB Al–steel butt welds revealed that the peak temperature at the Al–steel interface was about 400 °C in a weld where the IMP layer thickness was measured to be in the range of 0.2 to 0.9 μm. Since the IMP layer was found to be up to ~1 μm thick in the present study, it can be assumed that the average Al–steel interface temperature was comparable to that in the previous study.

All of the Al–Ti tensile specimens resulted in ductile fracture development in the Al FM, which implies that the intermixed and the IMP regions were thin enough to not initiate interfacial fracture. This conclusion is also consistent with previous studies that have reported that the critical IMP layer thicknesses that causes interfacial fracture in Al–Ti FSW joints are much larger, *e.g.*, ~5 μm[19] and ~10 μm.[18]

D. *The Interfacial Intermetallic Phases*

During dissimilar metal welding, the heating and high deformation enhance interdiffusion across the interface, which, in turn, leads to the formation of various IMPs, depending on the thermo-mechanical conditions and the chemical compositions of the alloys. Furthermore, the short time scales being characteristic of welding imply that the IMPs which form do not necessarily confine to those present in the corresponding phase diagrams which refer to the equilibrium phases. Therefore, also some reported metastable IMPs were considered as candidate phases in this work, as listed in Tables S-I to S-IV.

When it comes to the Al–Cu interface, the θ-Al_2Cu and the γ_1-Al_4Cu_9 phase were observed (Figure 4). The θ-Al_2Cu phase is the most Al-rich phase in the phase diagram,[42,46,47] and it is believed to have formed as Cu diffused into Al during the HYB process. On the opposite side of the phase diagram, the β phase is the most Cu-rich phase, but it is only stable at temperatures above 560 °C. There is also a Cu-rich α_2 (or α') phase but this has been found to appear first after several days of annealing at temperatures below about 360 °C.[42,46,47] The β and α_2 phases were, therefore, not considered as candidates in this study. The next most Cu-rich phase in the phase diagram is the γ_1-Al_4Cu_9 phase, which is believed to have formed following Al diffusion into the Cu BM. Several studies have reported that a layer of the Al_2Cu and the Al_4Cu_9 phase forms at Al–Cu interfaces.[12,69–71] Further, several studies have reported that a thinner layer of AlCu[68,72] or of both AlCu and Al_4Cu_3[23,73] may form between Al_2Cu and Al_4Cu_9 following prolonged IMP layer growth. This corresponds well with the thinner middle layer observed for thicker IMP layer regions in the present study.

At the Al–steel interface, the cubic α_c-Al–(Fe,Cu)–Si phase, the θ-Fe_4Al_{13} phase and the η-Fe_2Al_5 phase were identified (Figure 6). The Si contained within the IMP layer originates from the Al FM. It is well known that Si influences the IMP formation and growth at Al–steel interfaces, typically resulting in a reduction in the IMP layer growth rate and formation of Al–Fe–Si phases.[74–77] Several stable and metastable Al–Fe[78,79] and Al–Fe–Si[80–82] phases have been reported, and those considered as candidates in this work are listed in Tables S-II and S-III. The cubic α_c phase is a metastable phase in the Al–Fe–Si system, where the hexagonal τ_5-$Al_{7.1}Fe_2Si$ phase (α_h, $P6_3/mmc$ (194), $a = 12.404$, $c = 26.234$ Å[83]) is the stable phase. However, the cubic α_c phase generally forms instead of the hexagonal τ_5-$Al_{7.1}Fe_2Si$ phase in the presence of certain transition elements denoted M, such as Mn, Cr, and Cu,

which may substitute for Fe.[84,85] The α_c phase can, thus, form with a range of compositions which affects the lattice parameter (Table S-III). Moreover, the space group $Pm\bar{3}$ has been reported at Fe/M ratios lower than ~1, while $Im\bar{3}$ has been reported at higher ratios.[86,87] In the present study, the Fe/M ratio is high, which supports the formation of the α_c phase with the space group $Im\bar{3}$. The same phase was also identified as the main phase present inside the IMP layers in the second- and third-generation Al–steel HYB joints, where the same Al FM was used.[35,36] Further, the θ-Fe_4Al_{13} and the η-Fe_2Al_5 phases were observed towards the steel side. These are Al-rich stable phases in the Al–Fe phase diagram that have been found at Al–Fe interfaces in numerous studies.[8,10,11,21,75,76,88–90] Other studies on IMP layers in Al–steel welds have also reported the phase sequence observed here (α_c, θ, η) when Mn and/or Cr is present,[75,88–91] which is consistent with the present findings. Interestingly, Cu was also detected in the Al–steel IMP layer (Figure 6(b)). The main source of Cu is believed to be detached Cu BM fragments stirred into the Al FM (Figure 2(d)). Local variations in the distribution of Cu fragments likely lead to similar fluctuations in the Cu content in the IMP layer. In a previous study, it was reported that both the hardness and the growth rate of the IMP layer may be reduced by adding Cu to the Al FM,[92] which means that the presence of Cu could be beneficial.

The Ti(Al,Si)$_3$ phase was observed at the Al–Ti interface (Figure 8). In the Al–Ti(–Si) system, several stable and metastable phases have been reported together with superstructures,[93] and the candidate phases considered in this work are listed in Table S-IV. In previous studies, Si has been reported to segregate to the Al–Ti interface prior to the formation of IMPs,[94] because of chemical attraction[95] combined with the relatively high diffusion rate of Si in Al.[94] Following interdiffusion, the $TiAl_3$ phase forms, as has been reported in several studies.[14,96] This phase is the most Al-rich phase in the Al–Ti phase diagram and is stable below about 735 °C.[93] It is often referred to as Ti(Al,Si)$_3$ since it may incorporate Si, in particular up to 16.4 at. pct at 550 °C,[97] which reduces its growth rate.[18,96] Another phase, τ_1-$Ti_7Al_5Si_{12}$, has also been reported to form together with Ti(Al,Si)$_3$ for Al alloys containing higher Si levels, *e.g.*, 3 to 10 wt pct[96] and 12 wt pct.[95,98] Here, the Si content in the Al–Ti–Si IMP layer was estimated to be $\gtrsim 10$ at. pct, and the Al FM contained 1.11 wt pct Si (Table I), which both support formation of Ti(Al,Si)$_3$.

V. SUMMARY AND CONCLUSIONS

Through examination of an Al–Cu–steel–Ti demonstration joint, this work explores the prospects of solid-state multi-material welding by the HYB method. Each of the three dissimilar metal interface regions in the joint were characterized with respect to interface microstructure and tensile properties. The main findings are summarized as follows:

1. Cu and Al were seen to bond in some areas, and TEM revealed a ~0.5 µm thick IMP layer that consisted mainly of the phases Al_2Cu and Al_4Cu_9. Several regions suffered from lack of bonding arising from insufficient supply of Al FM, which caused the miniature Al–Cu tensile test specimens to fracture during machining or mounting in the test machine. Placing Cu on the AS instead of on the RS could solve this problem and allow manufacturing of sound Al–Cu HYB butt joints.

2. Between steel and Al no gaps or pores were observed, and IMP layers were found together with several microscale intermixed Al–steel regions. TEM of the interface region in the middle of the weld groove showed a ~0.1 to 1 µm thick Al–Fe–Si(–Cu) IMP layer that consisted of the phases α_c-Al–(Fe,Cu)–Si, θ-Fe_4Al_{13} and η-Fe_2Al_5. During tensile testing of miniature specimens ($\varnothing$1.0 mm), brittle fracture occurred along the interface, and the average UTS was measured to be 257 ± 35 MPa. Altogether, HYB showed great promise for Al–steel joining.

3. Al and Ti were successfully bonded, and TEM revealed some intermixed swirl-like regions that were a few µm thick, together with a ~50 nm thick Al–Ti–Si IMP layer. SPED revealed that the IMP layer contained the $Ti(Al,Si)_3$ phase. During tensile testing of miniature specimens, ductile fracture occurred in Al, and the UTS was measured to be 306 ± 2 MPa. The excellent tensile properties are believed to be a result of the combined action of a low process temperature contributing to a thin IMP layer and a favorable placement of Ti on the AS, where the down-flow of the Al FM is more vigorous.

In total, the HYB method shows great potential for dissimilar metal welding involving bonding of Al to Cu, steel, and Ti, which should be further explored in future studies.

ACKNOWLEDGMENTS

CONFLICT OF INTEREST

On behalf of all authors, the corresponding author states that there is no conflict of interest.

FUNDING

OPEN ACCESS

SUPPLEMENTARY INFORMATION

The online version of this article (https://doi.org/10.1007/s11661-023-07047-3) contains supplementary material, which is available to authorized users.

REFERENCES

1. K. Martinsen, S.J. Hu, and B.E. Carlson: *CIRP Ann. Manuf. Technol.*, 2015, vol. 64, pp. 679–99.
2. H. Wargnier, F.X. Kromm, M. Danis, and Y. Brechet: *Mater. Des.*, 2014, vol. 56, pp. 44–49.
3. J. Naito and R. Suzuki: *Kobelco Technol. Rev.*, 2020, vol. 38, pp. 32–37.
4. M. Tisza and I. Czinege: *Int. J. Lightweight Mater. Manuf.*, 2018, vol. 1(4), pp. 229–38.
5. A. Gloria, R. Montanari, M. Richetta, and A. Varone: *Metals*, 2019, vol. 9(6), pp. 1–26.
6. J.C. Williams and R.R. Boyer: *Metals*, 2020, vol. 10(6), pp. 1–22.
7. M.S.M. Isa, K. Moghadasi, M.A. Ariffin, S. Raja, M.R. Bin Muhamad, F. Yusof, M.F. Jamaludin, N. Bin Yusoff, and M.S. Bin Ab Karim: *J. Mater. Res. Technol.*, 2021, vol. 15, pp. 2735–80.
8. H. Springer, A. Kostka, J.F. dos Santos, and D. Raabe: *Mater. Sci. Eng. A*, 2011, vol. 528(13–14), pp. 4630–42.
9. P. Xue, B.L. Xiao, and Z.Y. Ma: *Metall. Mater. Trans. A*, 2015, vol. 46A(7), pp. 3091–3103.
10. A. Bahadur and O.N. Mohanty: *Mater. Trans. JIM*, 1991, vol. 32(11), pp. 1053–61.
11. K. Bouche, F. Barbier, and A. Coulet: *Mater. Sci. Eng. A*, 1998, vol. 249(1–2), pp. 167–75.
12. H.G. Jiang, J.Y. Dai, H.Y. Tong, B.Z. Ding, Q.H. Song, and Z.Q. Hu: *J. Appl. Phys.*, 1993, vol. 74(10), pp. 6165–69.
13. F.J.J. Van Loo and G.D. Rieck: *Acta Metall.*, 1973, vol. 21(1), pp. 61–71.
14. T. Enjyo, K. Ikeuchi, M. Kanai, and T. Maruyama: *Trans. JWRI*, 1977, vol. 6, pp. 123–30.

15. R. Borrisutthekul, T. Yachi, Y. Miyashita, and Y. Mutoh: *Mater. Sci. Eng. A*, 2007, vol. 467(1–2), pp. 108–13.
16. T. Tanaka, T. Morishige, and T. Hirata: *Scripta Mater.*, 2009, vol. 61(7), pp. 756–59.
17. W.B. Lee, K.S. Bang, and S.B. Jung: *J. Alloy. Compd.*, 2005, vol. 390(1–2), pp. 212–19.
18. A. Fuji, K. Ameyama, and T.H. North: *J. Mater. Sci.*, 1995, vol. 30(20), pp. 5185–91.
19. Y.C. Kim and A. Fuji: *Sci. Technol. Weld. Joining*, 2002, vol. 7(3), pp. 149–54.
20. M. Abbasi, A. Karimi Taheri, and M.T. Salehi: *J. Alloy. Compd.*, 2001, vol. 319(1–2), pp. 233–41.
21. S. Kobayashi and T. Yakou: *Mater. Sci. Eng. A*, 2002, vol. 338(1–2), pp. 44–53.
22. Y. Funamizu and K. Watanabe: *Trans. J.*, 1971, vol. 12, pp. 147–52.
23. C.Y. Chen and W.S. Hwang: *Mater. Trans.*, 2007, vol. 48(7), pp. 1938–47.
24. L. Xu, Y.Y. Cui, Y.L. Hao, and R. Yang: *Mater. Sci. Eng. A*, 2006, vol. 435–436, pp. 638–47.
25. W. Cai, G. Daehn, A. Vivek, J. Li, H. Khan, R.S. Mishra, and M. Komarasamy: *J. Manuf. Sci. E. T. ASME*, 2019, vol. 141(3), pp. 1–35.
26. Heidarzadeh, A., Mironov, S., Kaibyshev, R., C, am, G., Simar, A., Gerlich, A., Khodabakhshi, F., Mostafaei, A., Field, D.P., Robson, J.D., Deschamps, A., Withers, P.J.: Friction stir welding/ processing of metals and alloys: A comprehensive review on microstructural evolution. Progress in Materials Science (March 2019) (2020).
27. O. Grong: *Weld. J.*, 2012, vol. 91(1), pp. 26–33.
28. O. Grong, L. Sandnes, and F. Berto: *Mater. Design Process. Commun.*, 2019, vol. 1(2), p. 41.
29. Grong, O.: Patent: Method and devices for joining of metal components, particularly light metal components. Patent US7131567B2 (2006).
30. U.R. Aakenes, O. Grong, and T. Austigard: *Mater. Sci. Forum*, 2014, vol. 794–796, pp. 339–44.
31. L. Sandnes, O. Grong, J. Torgersen, T. Welo, and F. Berto: *Int. J. Adv. Manuf. Technol.*, 2018, vol. 98(5–8), pp. 1059–65.
32. O. Grong, L. Sandnes, and F. Berto: *Proc. Struct. Integr.*, 2019, vol. 17, pp. 788–98.
33. J. Blindheim, T. Welo, and M. Steinert: *Int. J. Adv. Manuf. Technol.*, 2019, vol. 105(5–6), pp. 2523–30.
34. F. Berto, L. Sandnes, F. Abbatinali, O. Grong, and P. Ferro: *Procedia Struct. Integr.*, 2018, vol. 13, pp. 249–54.
35. T. Bergh, L. Sandnes, D. Neal, F. Berto, R. Holmestad: Mater. Charact. 2021, p. 110761.
36. L. Sandnes, T. Bergh, O. Grong, R. Holmestad, P.E. Vullum, and F. Berto: *Mater. Sci. Eng. A*, 2021, vol. 809, p. 140975.
37. L. Sandnes, T. Welo, O. Grong, and F. Berto: On the fatigue properties of a third generation aluminium-steel butt weld made by hybrid metal extrusion bonding (hyb). *Int. J. Fatigue*, 2022, vol. 155, pp. 62–67.
38. ASTM International: ASTM E92-17 Standard Test Methods for Vickers Hardness and Knoop Hardness of Metallic Materials (2017). https://www.astm.org/e0092-17.html.
39. J. Blindheim, O. Grong, T. Welo, and M. Steinert: *J. Mater. Process. Technol.*, 2020, vol. 282, p. 116684.
40. de la Pena, F., Prestat, E., Fauske, V.T., Burdet, P., Jokubauskas, P., Nord, M., Ostasevicius, T., MacArthur, K.E., Sarahan, M., Johnstone, D.N., Taillon, J., Lahnemann, J., Migunov, V., Eljarrat, A., Caron, J., Aarholt, T., Mazzucco, S., Walls, M., Slater, T., Winkler, F., Pquinn-dls, Martineau, B., Donval, G., McLeod, R., Hoglund, E.R., Alxneit, I., Lundeby, D., Henninen, T., Zagonel, L.F., Garmannslund, A.: hyperspy/hyperspy: Hyperspy v1.5.2. Zenodo. https://doi.org/10.5281/ZENODO.3396791.
41. Johnstone, D., Crout, P., Nord, M., Francis, C., Laulainen, J., Hogas, S., Opheim, E., Martineau, B., Bergh, T., Prestat, E., Cautaerts, N., Smeets, S., ◦Anes, H.W., Ross, A., Broussard, J., Collins, S., Furnival, T., Jannis, D., Hjorth, I., Danaie, M., Herzing, A., Jacobsen, E., Poon, T., Doherty, T., Huang, S., Morzy, J., Iqbal, A., Ostasevicius, T., von Lany, M., Tovey, R.: pyxem/pyxem: pyxem 0.14.2. Zenodo (2022). https://doi.org/10.5281/ZENODO.6645923.
42. J.L. Murray: *Int. Metals Rev.*, 1985, vol. 30(5), pp. 211–33.
43. E.E. Havinga: *J. Less-Common Metals*, 1972, vol. 27(2), pp. 187–93.
44. S. Westman: *Acta Chem. Scand.*, 1965, vol. 19(6), pp. 1411–19.
45. E.H. Kisi and J.D. Browne: *Acta Crystallogr. B*, 1991, vol. 47(6), pp. 835–43.
46. N. Ponweiser, C.L. Lengauer, and K.W. Richter: *Intermetallics*, 2011, vol. 19(11), pp. 1737–46.
47. O. Zobac, A. Kroupa, A. Zemanova, and K.W. Richter: *Metall. Mater. Trans. A*, 2019, vol. 50A(8), pp. 3805–15.
48. M. Cooper: *Acta Crystallogr. A*, 1967, vol. 23, pp. 1106–07.
49. A. Raman and K. Schubert: *Z. Metallk.*, 1965, vol. 56, pp. 1–8.
50. P. Villars (ed.): TiAl3 Crystal Structure: Datasheet from "PAULING FILE Multinaries Edition–2012". Springer. https://materials.springer.com/isp/crystallographic/docs/sd0261474.
51. S. Chen, Y. Han, X. Jiang, X. Li, T. Yuan, W. Jiang, and X. Wang: *J. Mater. Process. Technol.*, 2021, vol. 297, 117205.
52. T. DebRoy and H.K.D.H. Bhadeshia: *Sci. Technol. Weld. Joining*, 2010, vol. 15(4), pp. 266–70.
53. A. Simar and M.-N. Avettand-Fenoel: *Sci. Technol. Weld. Joining*, 2017, vol. 22(5), pp. 389–403.
54. A. Elkjaer, J.A. Sorhaug, G. Ringen, R. Bjorge, and O. Grong: *J. Manuf. Process.*, 2022, vol. 79(April), pp. 626–38.
55. I. Galvao, R.M. Leal, A. Loureiro, and D.M. Rodrigues: *Sci. Technol. Weld. Joining*, 2010, vol. 1718, pp. 654–60.
56. P. Xue, D.R. Ni, D. Wang, B.L. Xiao, and Z.Y. Ma: *Mater. Sci. Eng. A*, 2011, vol. 528(13–14), pp. 4683–89.
57. F. Leoni, O. Grong, L. Sandnes, T. Welo, and F. Berto: *J. Adv. Joining Process.*, 2020, vol. 1, 100006.
58. F. Leoni, O. Grong, A. Celotto, H.G. Fjar, P. Ferro, and F. Berto: *Metals*, 2022, vol. 12(1656), pp. 1–23.
59. R.S. Coelho, A. Kostka, J.F. dos Santos, and A. Kaysser-Pyzalla: *Mater. Sci. Eng. A*, 2012, vol. 556, pp. 175–83.
60. H. Das, K.J. Lee, and S.T. Hong: *J. Mater. Eng. Perform.*, 2017, vol. 26(7), pp. 3607–13.
61. M. Mahmoudiniya, A.H. Kokabi, S. Kheirandish, and L.A.I. Kestens: *Mater. Sci. Eng. A*, 2018, vol. 737(September), pp. 213–22.
62. A. Kar, S. Suwas, and S.V. Kailas: *Metall. Mater. Trans. A*, 2019, vol. 50A, pp. 5153–73.
63. L.E. Murr, Y. Li, R.D. Flores, E.A. Trillo, and J.C. McClure: *Mater. Res. Innovat.*, 1998, vol. 2, pp. 150–63.
64. U. Dressler, G. Biallas, and U. Alfaro Mercado: *Mater. Sci. Eng. A*, 2009, vol. 526(1–2), pp. 113–17.
65. A. Wu, Z. Song, K. Nakata, J. Liao, and L. Zhou: *Mater. Des.*, 2015, vol. 71, pp. 85–92.
66. A. Elrefaey, M. Gouda, M. Takahashi, and K. Ikeuchi: *J. Mater. Eng. Perform.*, 2005, vol. 14(1), pp. 10–17.
67. P. Xue, B.L. Xiao, D. Wang, and Z.Y. Ma: *Sci. Technol. Weld. Joining*, 2011, vol. 16(8), pp. 657–61.
68. H. Xu, I. Qin, H. Clauberg, B. Chylak, and V.L. Acoff: *Scripta Mater.*, 2016, vol. 115, pp. 1–5.
69. P. Xue, B.L. Xiao, D.R. Ni, and Z.Y. Ma: *Mater. Sci. Eng. A*, 2010, vol. 527(21–22), pp. 5723–27.
70. H. Xu, C. Liu, V.V. Silberschmidt, S.S. Pramana, T.J. White, Z. Chen, and V.L. Acoff: *Acta Mater.*, 2011, vol. 59(14), pp. 5661–73.
71. I. Galvao, A. Loureiro, and D.M. Rodrigues: *Sci. Technol. Welding Joining*, 2016, vol. 21(7), pp. 523–46.
72. K.S. Lee, S. Lee, J.S. Lee, Y.B. Kim, G.A. Lee, S.P. Lee, and D.S. Bae: *Met. Mater. Int.*, 2016, vol. 22(5), pp. 849–55.
73. E. Hug and N. Bellido: *Mater. Sci. Eng. A*, 2011, vol. 528(22–23), pp. 7103–06.
74. D.I. Layner and A.K. Kurakin: *Fiz. Metal. Metalloved.*, 1964, vol. 18(1), pp. 145–48.
75. L.A. Jacome, S. Weber, A. Leitner, E. Arenholz, J. Bruckner, H. Hackl, and A.R. Pyzalla: *Adv. Eng. Mater.*, 2009, vol. 11(5), pp. 350–58.
76. W.-J. Cheng and C.-J. Wang: *Mater. Charact.*, 2010, vol. 61(4), pp. 467–73.
77. H. Springer, A. Kostka, E.J. Payton, D. Raabe, A. Kaysser-Pyzalla, and G. Eggeler: *Acta Mater.*, 2011, vol. 59(4), pp. 1586–1600.
78. U.R. Kattner and B.P. Burton: *ASM Metals Handb.*, 1992, vol. 3, pp. 294–95.

79. X. Li, A. Scherf, M. Heilmaier, and F. Stein: *J. Phase Equilib. Diffus.*, 2016, vol. 37(2), pp. 162–73.
80. N. Krendelsberger, F. Weitzer, and J.C. Schuster: *Metall. Mater. Trans. A*, 2007, vol. 38A, pp. 1681–91.
81. G. Ghosh: *Phys. Chem.*, 2008, vol. 11D1, pp. 1–83.
82. M.C.J. Marker, B. Skolyszewska-Kuhberger, H.S. Effenberger, C. Schmetterer, and K.W. Richter: *Intermetallics*, 2011, vol. 19(12), pp. 1919–29.
83. R.N. Corby and P.J. Black: *Acta Crystallogr. A*, 1977, vol. B33, pp. 3468–75.
84. D. Munson: *J. Inst. Met.*, 1967, vol. 95, pp. 217–19.
85. C.Y. Sun and L.F. Mondolfo: *J. Inst. Met.*, 1967, vol. 95, p. 384.
86. A.L. Dons: *Zeitschrift fur Metallkunde*, 1985, vol. 76(2), pp. 151–53.
87. P. Donnadieu, G. Lapasset, and T.H. Sanders: *Philos. Magn. Lett.*, 1994, vol. 70(5), pp. 319–26.
88. S.M. Arbo, T. Bergh, H. Solhaug, I. Westermann, and B. Holmedal: *Procedia Manuf.*, 2018, vol. 15, pp. 152–60.
89. J. Chen, B. Shalchi Amirkhiz, R. Zhang, and B. Rona: *Metall. Mater. Trans. A*, 2020, vol. 51A(10), pp. 5198–12.
90. T. Bergh, S.M. Arbo, A. Brocks, J. Friis, M. Zeeshan, I. Gudem, R. Holmestad, I. Westermann, and P. Erik: *Intermetallics*, 2022, vol. 142, 107443.
91. T. Bergh, H.W. Anes, R. Aune, S. Wenner, R. Holmestad, X. Ren, and P.E. Vullum: *Mater. Trans.*, 2023, vol. 64(2), pp. 352–59.
92. J.L. Song, S.B. Lin, C.L. Yang, C.L. Fan, and G.C. Ma: *Sci. Technol. Weld. Joining*, 2010, vol. 15(3), pp. 213–18.
93. J. Braun and M. Ellner: *Metall. Mater. Trans. A*, 2001, vol. 32A(5), pp. 1037–47.
94. C. Zhang, J.D. Robson, S.J. Haigh, and P.B. Prangnell: *Metall. Mater. Trans. A*, 2019, vol. 50A, pp. 5143–52.
95. S.-H. Chen, L.-Q. Li, Y.-B. Chen, and D.-J. Liu: *Trans. Nonferrous Metals Soc. China*, 2010, vol. 20(1), pp. 64–70.
96. T. Takemoto and I. Okamoto: *J. Mater. Sci.*, 1988, vol. 23(4), pp. 1301–08.
97. J. Wang, Y. Liu, Y. Liu, C. Wu, and X. Su: *J. Phase Equilib. Diffus.*, 2019, vol. 40(6), pp. 810–19.
98. S. Chen, L. Li, Y. Chen, and J. Huang: *J. Alloy Compd.*, 2011, vol. 509(3), pp. 891–98.